nature communications

Article

https://doi.org/10.1038/s41467-024-54690-4

Coordination between deformation, precipitation, and erosion during orogenic growth

Received: 19 February 2024

Accepted: 18 November 2024

Published online: 28 November 2024

Check for updates

Xiaoping Yuan[1] ✉, Yuqiang Li[1], Sascha Brune[2,3], Kai Li[2,4], Michaël Pons[2] & Sebastian G. Wolf[2,5]

Crustal thickening associated with orogenic growth elevates topography, causing orographic enhancement of precipitation, which in turn facilitates local erosion and possibly intensifies localization of deformation. How these three processes—deformation, precipitation, and erosion—coordinate during orogenic growth remains unknown. Here, we present a numerical model where tectonics, surface processes, and orographic precipitation are tightly coupled, and explore the impact on low, intermediate, and high erodibility orogens. We show that, for intermediate erodibility models, rock uplift rates and precipitation rates correlate well with erosion rates during the formation of orogenic plateaus with high correlation coefficients of ~0.9 between rock uplift and erosion rates, and ~0.8 between precipitation and erosion rates. We demonstrate a cyclicity of correlation evolution among uplift, precipitation, and erosion rates through the development of new faults propagating outward. These results shed insights into the relative tectonic or climatic control on erosion in active orogens (e.g., Himalayas, Central Andes, and Southern Alps of New Zealand), and provide a plausible explanation for several conflicting data and interpretations in the Himalayas, which depend on the stage of maturity of the newest fault and the relative locations to old faults.

In convergent orogens, deformation, surface uplift, and erosion closely interact: deformation induces surface uplift, and surface uplift leads to an increase in erosion rate through orographic enhancement of precipitation[1–4]. Mountain height and shape thus result from the interrelationship between tectonic uplift, uplift-enhanced precipitation, and erosion. The orographic climate-tectonics-erosion feedback exists in small orogens such as the Southern Alps of New Zealand (SANZ) and Olympic Mountains of Washington State, USA[1,5], and may be even stronger under some circumstances in active orogens on the margins of large, high-elevation plateaus such as the Himalayas, the Tibetan Plateau, and the Central Andes[1–4,6]. Uplift-enhanced precipitation causes rapid erosion, denudation, and thus weakening of the orogenic margins which intensifies the localization of the deformation[7–9]. The notion of tectonics-climate-erosion coupling and feedbacks has been repeatedly proposed and challenged over the past two decades[2,10–14] and remains one of the largest uncertainties in Earth science research.

Along the Himalayas, between roughly 77° and 87° E longitude, there is a general correlation between high rainfall, high relief, and rapid exhumation recorded in young apatite fission-track ages[2,8,11]. This causes an entrenched debate about climatic and tectonic controls on localization of strain and erosion[2,8–13,15] mainly because the orographic enhancement of precipitation likely produces spatial correlations between enhanced precipitation and rapid rock uplift, even in the

[1]State Key Laboratory of Biogeology and Environmental Geology, Hubei Key Laboratory of Critical Zone Evolution, School of Earth Sciences, China University of Geosciences, Wuhan, China. [2]Helmholtz Centre Potsdam - GFZ German Research Centre for Geosciences, Potsdam, Germany. [3]Institute of Geosciences, University of Potsdam, Potsdam, Germany. [4]Institute of Geological Sciences, Freie Universität Berlin, Berlin, Germany. [5]Department of Earth Science, University of Bergen, Bergen, Norway. ✉e-mail: yuanxiaoping@cug.edu.cn

absence of a tectonic response to climate and erosion. A related more fundamental question is why do orogenic systems 'self-organize' such that all three processes—deformation, precipitation, and erosion—appear to be correlated in active orogens?[10]. Since nature does not provide ideal experiments to test these hypotheses, interpretations of spatial correlations among topography, precipitation, erosion, and active deformational structures are speculative[2]. Consequently, demonstration of a cause-and-effect relationship among these processes remains elusive.

Previous numerical models study how feedback between erosion and rheology may alter climate-tectonic interactions by using a simplified uniform erosion efficiency[16,17] or by imposing a kinematic denudation focused on one side of orogenic topography[1,7,18]. These simplifications neglect important dynamic feedbacks among deformation, orographic precipitation, and erosion during mountain building, and thus the response of large orogenic systems to spatio-temporally tectonic and climatic change has not yet been systematically explored. One way of testing and disentangling the proposed links among deformation, climate, and erosion is to have a physics-based evolutionary model that couples deformation, climate, and surface processes[1,2,7,17,19,20].

In this work, we present a coupled model that links three codes specialized in modeling tectonics, surface processes, and orographic precipitation. We address one fundamental question with three (low, intermediate, and high) erodibility models: How do deformation, orographic precipitation, and erosion coordinate during orogenic growth? Then we show how the intermediate erodibility models and correlation among deformation, precipitation, and erosion evolve in detail, and how they compare to observations.

Results

Model of coupled tectonics, surface process, and orographic precipitation

We use the thermo-mechanical tectonic model ASPECT[21–24] coupled with the landscape evolution model FastScape[25–27] and the physics-based orographic precipitation model LFPM[28] acting on the topographic surface, to resolve the interaction among tectonic deformation, surface processes, and orographic precipitation at a high resolution. ASPECT computes the non-linear brittle-plastic and ductile-viscous deformation of materials ("Methods"). FastScape solves for fluvial erosion, sediment transport and deposition, and hillslope processes. LFPM considers advection, dispersion, and interaction of water contents (i.e., vapor and cloud water) in atmosphere and fallout as orographic precipitation responding to topography ("Methods").

The erosional efficiency $K = K_f \tilde{p}^m$ ("Methods", Eq. 10) depends on rainfall and its variability $\tilde{p}$ [29], drainage area exponent m, and mostly on bedrock erodibility K_f, varying several orders of magnitude ($10^{-7} - 10^{-4} \mathrm{m}^{0.2}/\mathrm{yr}$) owing to its dependence on lithology, fracturation, vegetation cover, and abrasive agents[30–32]. We present three representative models with low erodibility ($K_f = 1 \times 10^{-6} \mathrm{m}^{0.2}/\mathrm{yr}$, Fig. 1a, b), medium erodibility ($1 \times 10^{-5} \mathrm{m}^{0.2}/\mathrm{yr}$, Fig. 1c, d), and high erodibility ($5 \times 10^{-5} \mathrm{m}^{0.2}/\mathrm{yr}$, Fig. 1e, f) over a large range of observed values.

We also test the regional climate and orographically enhanced precipitation in two cases[1]: dominant wind in the direction of subducting plate motion (Fig. 1a, c, and e), and the opposite direction of subducting plate motion (Fig. 1b, d, and f). For simplicity, we use the same influx of vapor and cloud water and the same length scales in all models (e.g., reference height, condensation length of vapor to cloud water, fallout length of cloud water, decay length, and dispersion length of precipitation, see "Methods"). The actual precipitation in different orogens (e.g., the Himalayas, the Central Andes, and the SANZ) depends on the above parameters, the dominant wind direction, and topographic evolution. Tests of the precipitation model with the influx and length-scale parameter values (see "Methods") agree with the maximum (~6 m/yr, Fig. 1a) and minimum (0.1 m/yr) precipitation rates that have been measured in the Himalaya-Tibet region[33]. Note that the Himalayas exhibit extraordinarily high precipitation due to the combined effects of Asian monsoon and orography. We run the orogenic growth model for 50 Myr with a constant convergence rate of v_c = 10 mm/yr (5 mm/yr on both model sides, Supplementary Fig. S1). The models in this work are not designed to reproduce the details of the geology and geometry of natural examples, and aim at the relations among rock uplift rates, precipitation rates, erosion rates, and exhumation, rather than their accurate magnitudes.

Three erodibility models and correlation analysis

In all models, shortening is accommodated by one-sided subduction of the lower crust and lithospheric mantle, and orogens grow through crustal thickening (Fig. 1, Supplementary Figs. S2–S4 and S8–S10, and Supplementary Movies 1-6). During convergence, low and medium erodibility models first grow to a maximum elevation of ~5 km, and then widen outward through thrust-faulting (Fig. 1a–d). For the low erodibility model, rock uplift and erosion rates are very low, and unbalanced at the active orogen margin (Fig. 1a, b). This case does not achieve an equilibrium between rock uplift and erosion rates, and it is in a transient growth stage. The orographic enhancement of precipitation occurs on the windward side of the orogen and retreats due to outward orogenic growth. However, the orographic precipitation does not efficiently affect rock uplift and erosion rates, nor the orogen cross-sectional geometry or exhumation rates (Fig. 1a, b).

For the medium erodibility model, both rock uplift and erosion rates are higher than those of the low erodibility model. They are balanced in the orogen center, but mostly unbalanced at the orogen margin above the new propagating faults (Fig. 1c, d). The cycles of propagating faults occur throughout orogenic growth, and the model does not reach an equilibrium between rock uplift and erosion rates throughout the 50-Myr model run. Orographic enhancement of precipitation increases the rock uplift and erosion rates and affects the geometry and shape of the orogen. In the medium erodibility model, the orientation of atmospheric moisture flux across the orogen influences its evolution, due to the orogen's elevation, which produces a strong orographic effect on precipitation. High exhumation rates occur across the topographic surface of the orogen on the windward side. A higher orographic precipitation rate causes a narrower orogen width on the pro-side of the orogen when the dominant wind is in the direction of subducting plate motion.

The high erodibility model exhibits a balance between rock uplift and erosion rates (Fig. 1e, f), and relatively constant orogen width (~100 km, Fig. 2c). In this case, we expect perpetual cycles of thrust inception and growth on the side of the subducting plate (Supplementary Fig. S4; Supplementary Movie 3). The small size of the orogen and specifics of the orographic model produce generally symmetric rainfall patterns, which makes the orogen fairly insensitive to the wind direction. Thus, the shape of this small orogen is not significantly affected by the dominant wind directions. Tests with slope exponent $n \neq 1$ in the stream power model do not significantly change our modeling results (see Supplementary Discussion, Supplementary Fig. S5), but there are some trade-offs between n values and the representative K_f values, consistent with previous findings[34].

We further show quantitative correlations among deformation, precipitation, and erosion by calculating the evolution of the Pearson correlation coefficient $R_{U\dot{e}}$ between rock uplift and erosion rates, and correlation coefficient $R_{P\dot{e}}$ between precipitation and erosion rates (see Methods for details). By testing various erodibilities in the observed range[30] and more complete correlation analyzes among deformation, precipitation, and erosion, we show that given our model setup and particular convergence rate, the correlation coefficients ($R_{U\dot{e}}$ and $R_{P\dot{e}}$) are low (<-0.25) when the erodibility is in the range of

https://doi.org/10.1038/s41467-024-54690-4

1×10^{-7}–1×10^{-6} $m^{0.2}$/yr. The correlations increase when the erodibility increases from 1×10^{-6} to 1×10^{-5} $m^{0.2}$/yr (Figs. 2 and S6). Above the medium erodibility of 1×10^{-5} $m^{0.2}$/yr, both correlation coefficients are relatively high (>~0.75). The correlation between the rock uplift and erosion rates is very high ($R_{U\dot{e}} \sim 1$) for erodibilities larger than 2×10^{-5} $m^{0.2}$/yr, to which narrow orogens will form rather than wide orogenic

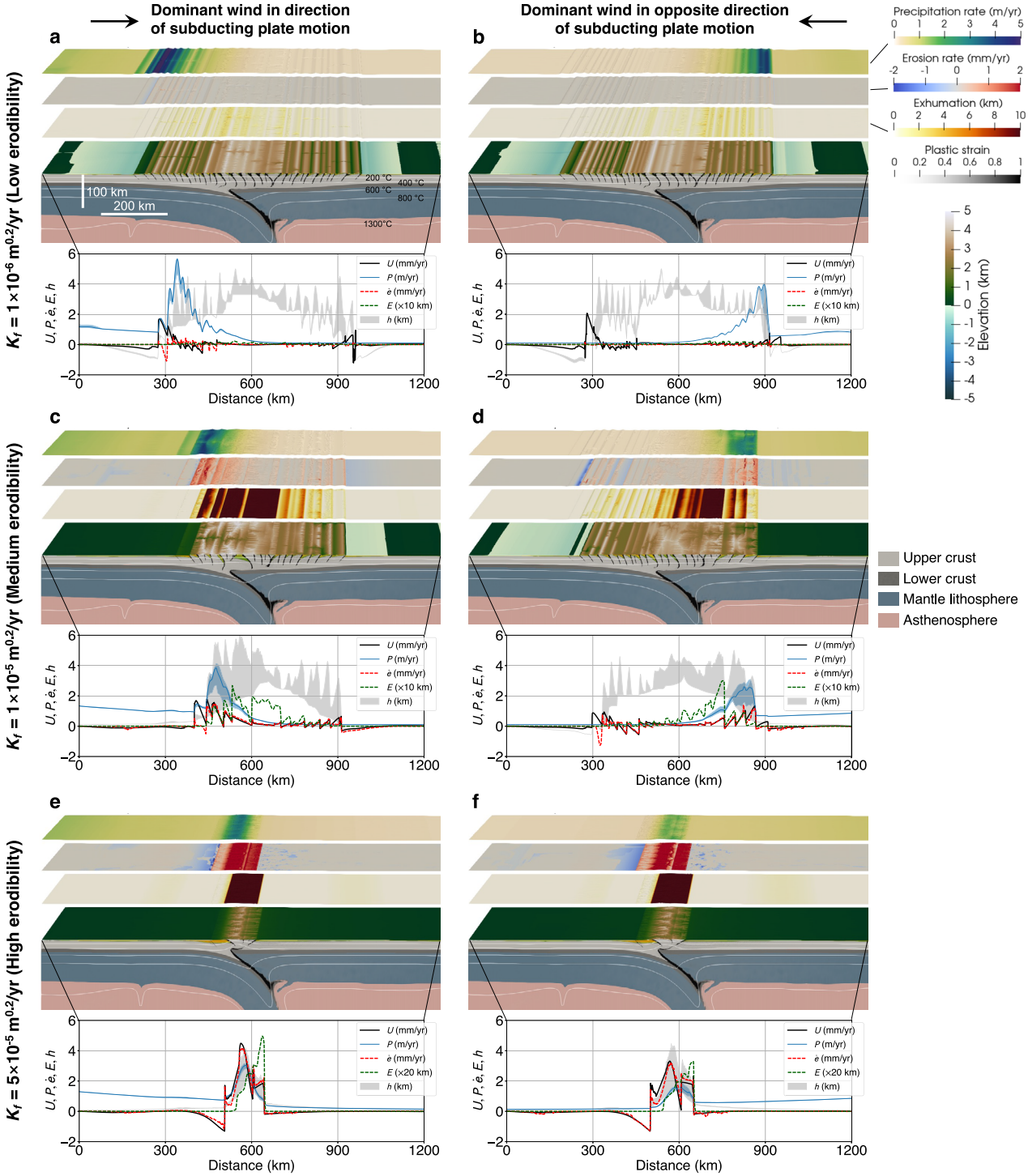

Fig. 1 | Model snapshots at the end of shortening (50 Myr) for cases with various erodibilities and two wind directions. The models account for three representative bedrock erodibilities (**a**, **b**) $K_f = 1 \times 10^{-6}$ $m^{0.2}$/yr (low), (**c**, **d**) 1×10^{-5} $m^{0.2}$/yr (medium), and (**e**, **f**) 5×10^{-5} $m^{0.2}$/yr (high). See Supplementary Movies 1 to 6 for temporal evolution. The dominant wind is aligned with the direction of subducting plate motion (left column), and the dominant wind is in the opposite direction of subducting plate motion (right column). For each panel, from top to bottom: map-view precipitation rate P (m/yr), erosion rate $\dot{e}$ (mm/yr), accumulated exhumation E (km), topographic elevation h (km), and the model domain showing the upper crust, lower crust, mantle lithosphere, and asthenosphere from the thermo-mechanical tectonic model (no vertical exaggeration). Swath elevation profile of landscape (h), the profile of rock uplift rate (U), the profile of minimum, average, and maximum precipitation rate (P), profiles of average erosion rate ($\dot{e}$) and average exhumation (E). The time step for calculating rock uplift and erosion rates corresponds to the time step in the tectonic model (~10000 yrs). For the cases of low (**a**, **b**) and high erodibilities (**e**, **f**), the dominant wind in the direction or the opposite direction of subducting plate motion does not change the shapes of the orogen. In contrast, with medium erodibility (**c**, **d**), the dominant wind direction modifies the shapes of orogen, but cannot stop the orogenic growth.

https://doi.org/10.1038/s41467-024-54690-4

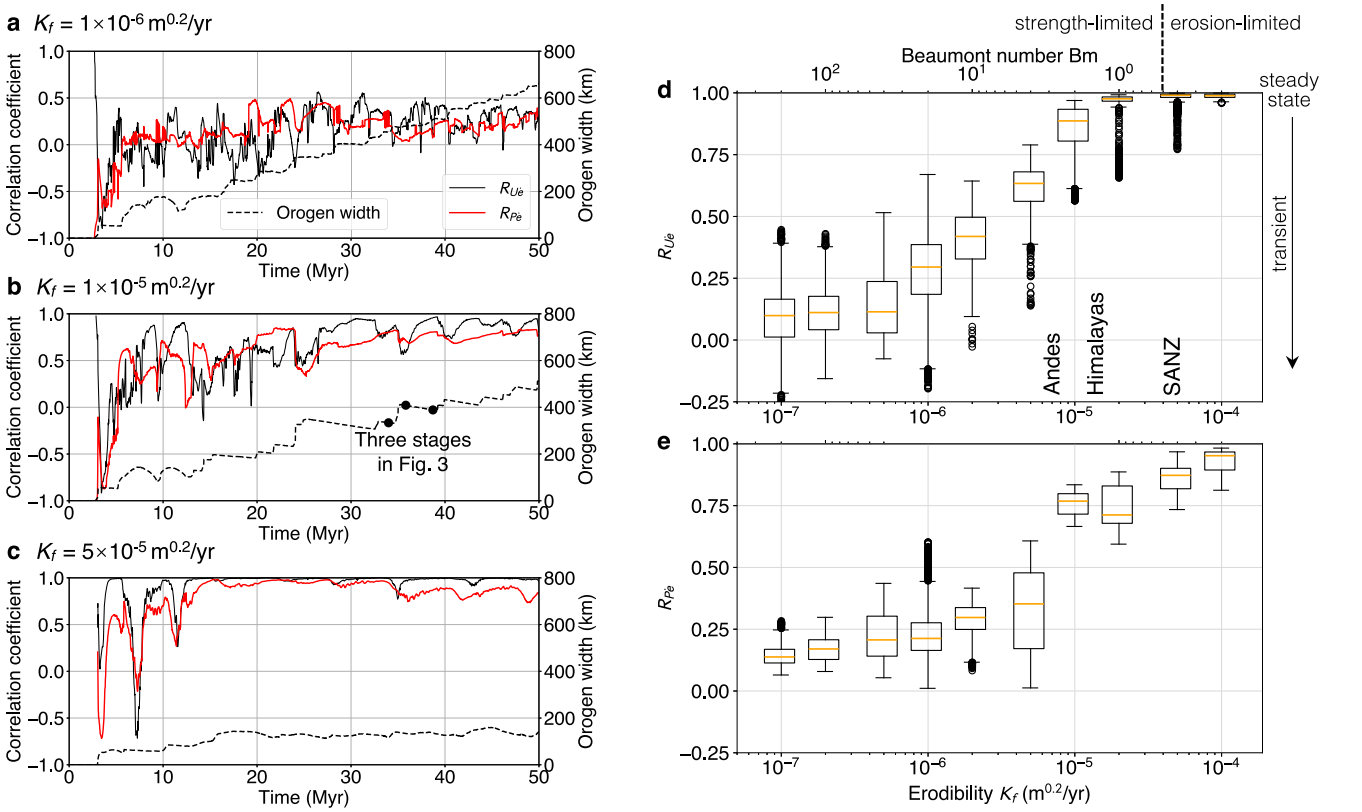

Fig. 2 | Pearson correlation coefficient $R_{U\dot{e}}$ between the uplift rate U and the erosion rate $\dot{e}$, and correlation coefficient $R_{P\dot{e}}$ between the precipitation rate P and the erosion rate $\dot{e}$. a–c Evolution of correlation coefficients ($R_{U\dot{e}}$ and $R_{P\dot{e}}$) and orogen width for three representative bedrock erodibilities (K_f = 1×10^{-6}, 1×10^{-5}, and 5×10^{-5} m$^{0.2}$/yr). The correlation coefficient and orogen width are calculated between two outermost orogenic points with topographic elevation above 500 m. The dominant wind aligns with the direction of subducting plate motion. In panel **b**, three dots correspond to three stages (34, 36, and 39 Myr) in Fig. 3. **d** Boxplot of correlation coefficient $R_{U\dot{e}}$ for 30–50 Myr model runs using bedrock erodibilities in the range of K_f = 1×10^{-7} –1×10^{-4} m$^{0.2}$/yr [30–32]. Median values are represented by the central orange lines; boxes extend from the 25th to 75th percentiles. The Andes, the Himalayas, and the SANZ are plotted according to the Beaumont numbers[17] (Bm, Supplementary Table S2), which characterize the orogen type (e.g., strength-limited for high Bm and erosion-limited for low Bm) and relative importance of tectonics and surface processes. The values of Bm are 1–2 (Himalayas)[17], 2–4 (Central Andes)[17], and 0.15–0.48 (SANZ)[17]. If correlation $R_{U\dot{e}}$ reaches 1, the associated processes are in flux steady state. If it is distinctly smaller, transient effects dominate. **e** Boxplot of correlation coefficient $R_{P\dot{e}}$ for 30–50 Myr model runs using bedrock erodibilities in the range of K_f = 1×10^{-7} – 1×10^{-4} m$^{0.2}$/yr. Both $R_{U\dot{e}}$ and $R_{P\dot{e}}$ are low for K_f in the range of 1×10^{-7} – 1×10^{-6} m$^{0.2}$/yr, increasing from 1×10^{-6} to 1×10^{-5} m$^{0.2}$/yr, and are relatively high for K_f > 1×10^{-5} m$^{0.2}$/yr.

plateaus (Fig. 1e, f, Supplementary Fig. S6). The correlation $R_{U\dot{e}}$ < 1 reflects an orogen in a transient growth stage (Fig. 2d), as also shown by the evolution of orogen width for different erodibilities (Fig. 2a, b, Supplementary Fig. S6). Rock uplift and erosion rates tend to be poorly correlated unless the orogen as a whole approaches a dynamic equilibrium between convergence and erosion fluxes.

Discussion

How do deformation, precipitation, and erosion coordinate during orogenic growth?

The relative importance of surface processes and tectonics can be quantified by the non-dimensional Beaumont number[17] (Bm, Supplementary Table S2), which characterizes the orogen type (e.g., strength-limited for high Bm and erosion-limited for low Bm). In collisional orogens, as modeled here, Bm is primarily determined by the plate convergence rate (v_c), the erodibility (K_f), and the crustal strength of colliding plates (F_{int}): Bm ∝ $v_c/(F_{int}K_f)$ (ref. 17). It is stressed that the values of v_c, K_f, and F_{int} in Bm are orogen-wide averages. We use the Beaumont number to further quantify our modeling results and to establish comparability with natural systems (Fig. 2d, e). The Himalayas are characterized by Bm =1–2 (ref. 17), which corresponds to an erodibility of 1×10^{-5}–2×10^{-5} m$^{0.2}$/yr in our modeling setup (Supplementary Table S2). The respective models with Bm = 1–2 have correlation coefficients of $R_{U\dot{e}} \sim 0.9 - 0.98$ and $R_{P\dot{e}} \sim 0.7 - 0.8$ (Fig. 2d, e). The strong correlations indicate that there can be a high degree of correlation even in non-steady state orogens. They also demonstrate a high degree of coordination between endogenic and exogenic processes, which in turn leads to a very predictable behavior such that if one process is quantified well, the others can be predicted at high accuracy.

We show further how deformation, precipitation, and erosion coordinate using the medium observed Bm = 2 (i.e., the erodibility of 1×10^{-5}m$^{0.2}$/yr) for the formation of the orogenic plateau as an example (Fig. 3). Several growth stages are shown (Figs. 2b and 3). In the early stage, the old fault and highly-elevated topography result in a single high-amount rainfall peak (Fig. 3a). In the youthful stage, a new fault emerges outboard of old faults, and the plateau grows outward. The uplift rate caused by the new fault is greater than the erosion rate because the landscape is not adjusted to the new uplift pattern. The orographic precipitation advances partially along with the elevated topography (Fig. 3b). In this stage, the evolving two-step morphology causes two rainfall peaks. In the mature stage, the topography continues growing until the rock uplift rate achieves a quasi-equilibrium with the erosion rate above the new fault. Subsequently, the topography reaches nearly its maximum elevation with a mature fault, partially forming one rainfall peak ahead (Fig. 3c). Finally, the orographic precipitation advances fully (i.e., a single rainfall peak forms) along with the highly-elevated topography, which returns to the old

https://doi.org/10.1038/s41467-024-54690-4

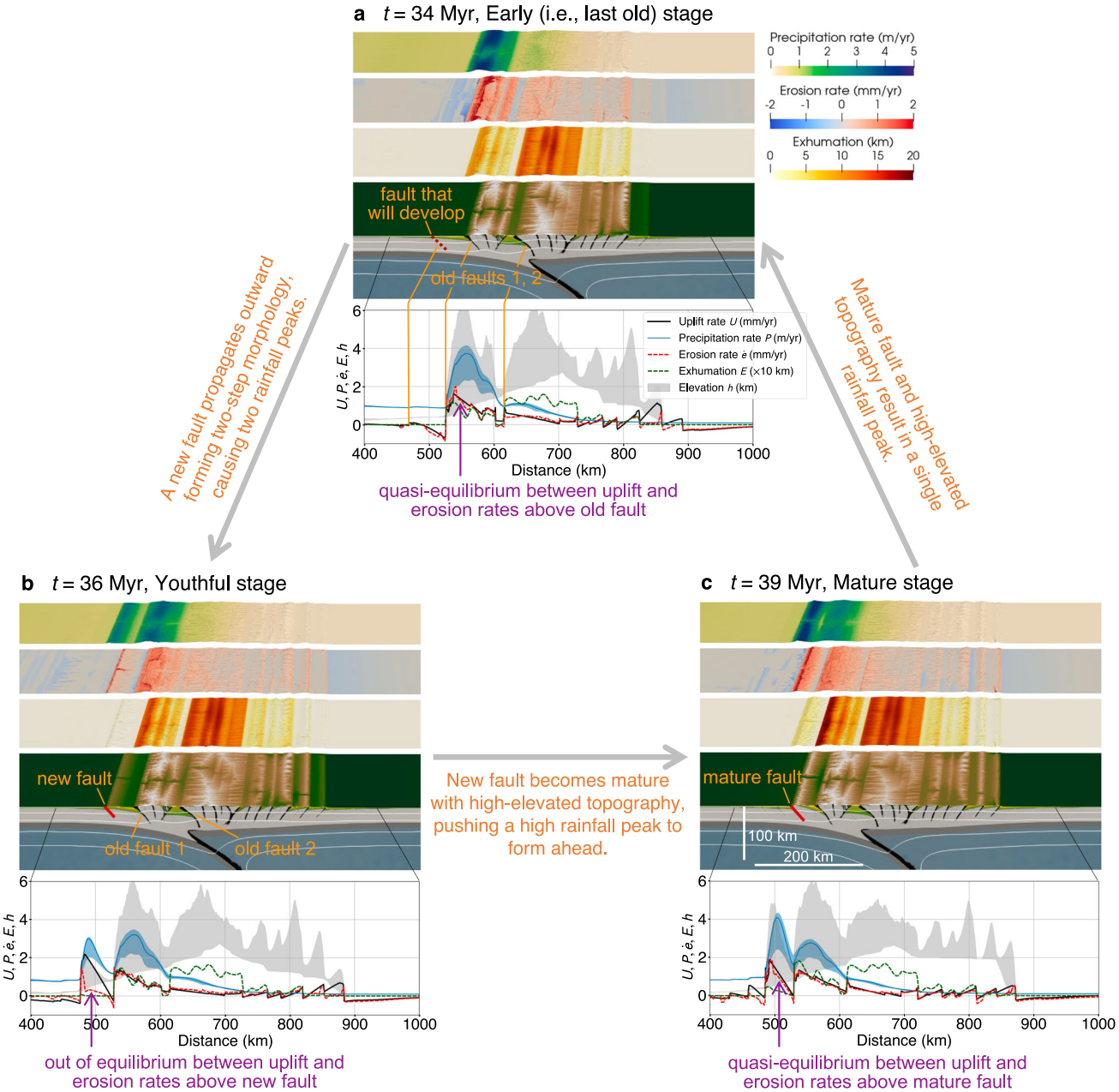

Fig. 3 | Cycle of correlation evolution among uplift rate *U*, precipitation rate *P*, and erosion rate *ė* in response to a new fault propagating outward. a Early (i.e., last old) stage: highly-elevated topography in the orogenic plateau margin forms a single rainfall peak, with quasi-equilibrium between uplift and erosion rates above the old fault. A new fault will develop outboard of old faults. **b** Youthful stage: a new fault propagates outward forming the two-step morphology, causing two rainfall peaks. Uplift and erosion rates are out of equilibrium above the new fault. **c** Mature stage: the new fault becomes mature (less active) with highly-elevated topography in the orogen margin during shortening, pushing a high rainfall peak to partially form ahead. Uplift and erosion rates reach quasi-equilibrium above the mature fault. The mature fault and highly-elevated topography result in a single rainfall peak to complete the cycle of correlation evolution among uplift, precipitation, and erosion.

stage forming a complete cycle of correlation evolution among rock uplift, precipitation, and erosion. Similar cycles are repeated when new faults propagate outward in front of old faults (Supplementary Fig. S7).

Our modeled phases and the orographic impact on rainfall distribution can be compared to the observations in the Himalayas, where two intrinsic end-members of topographic profiles are identified[33]: (i) in far western and eastern parts of the Himalayas, mean topography rises steadily to an average elevation of 5 km; (ii) in contrast, particularly in the central and central-western Himalayas, mean topographic profiles are characterized by a two-step morphology of which the outer step corresponds to the Lesser Himalaya and the inner step to the Greater Himalaya geologic units (Fig. 4d). These two types of topographic profiles are mimicked by the rainfall distribution, with a single, high peak of ~5–6 m/yr for the steadily increasing topography versus two peaks with lower amounts of ~3–4 m/yr for the two-step morphology[33]. Our modeled two-step topography with two rainfall peaks and one-step topography with one rainfall peak, forming respectively in the youthful (active) stage and the mature (less active) stage of a propagating fault in the orogenic plateau margin, are consistent with the two observed patterns in the Himalayas. We suggest that these two topographic and precipitation patterns are related to the maturity of the newest active thrust faults in the Himalayan front,

https://doi.org/10.1038/s41467-024-54690-4

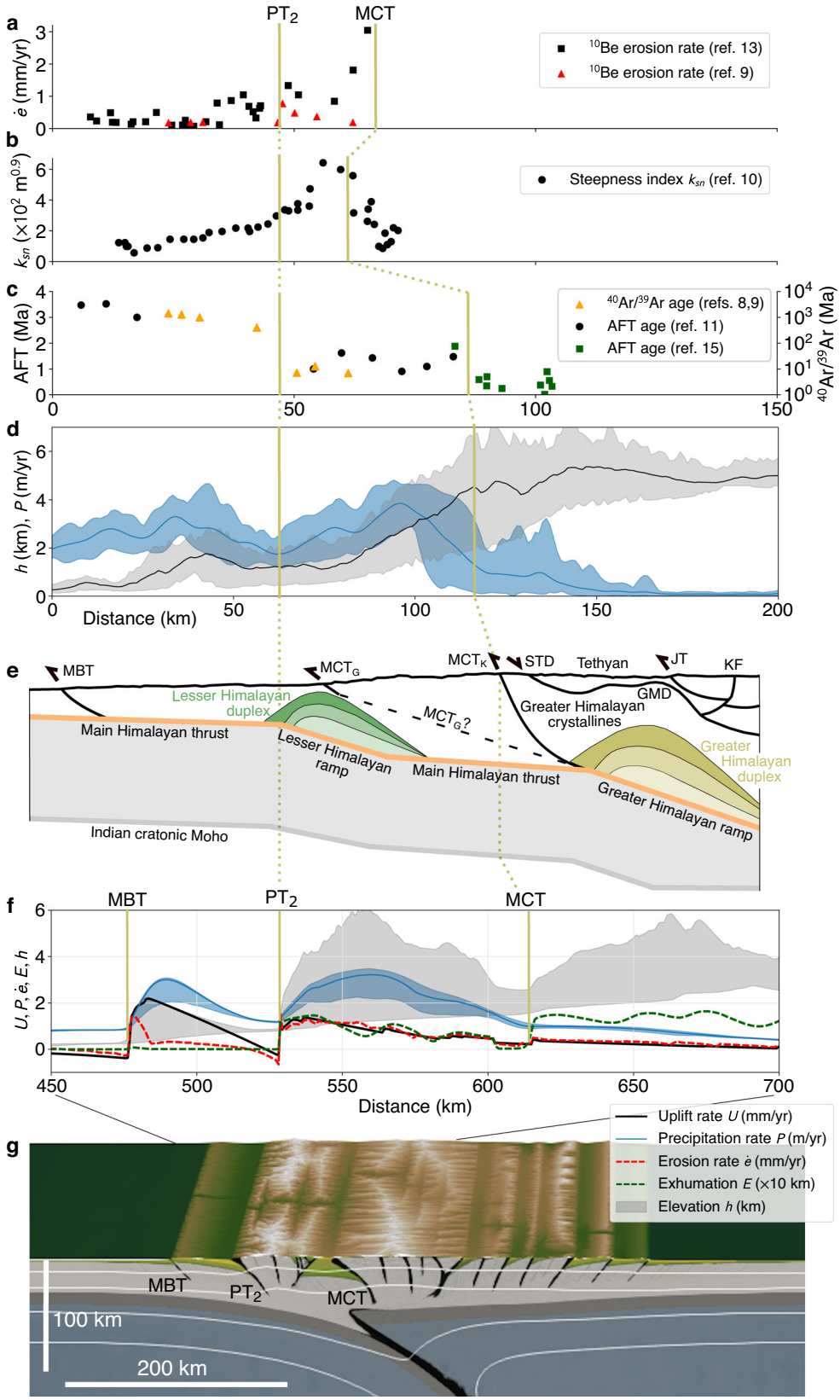

e.g., the Main Boundary Thrust (MBT) and/or the Main Frontal Thrust (MFT), with the mature stage (less active) in the far western and eastern parts of the Himalayas and the youthful stage (active) in the central and central-western Himalayas.

In contrast to the Himalayas, the Central Andes feature a Bm = 2–4 (ref. 17), which corresponds to an erodibility range of 5×10^{-6} – 1×10^{-5} $m^{0.2}$/yr (Supplementary Table S2) in our model setup. The corresponding ranges of correlation coefficients are $R_{U\dot{e}} \sim 0.65 - 0.9$, $R_{P\dot{e}} \sim 0.35 - 0.8$ (Fig. 2d, e). These values are distinctly smaller than those of the Himalayas, which implies that the Central Andes are further away from flux steady state than Himalaya-Tibet. This is attested by shallow levels of exhumation and low erosion rates in the Central

Fig. 4 | Comparison of the observed and the modeled erosion patterns in the Himalayas separated by several major faults. a Cosmogenic ^{10}Be erosion rates (triangle symbols, ref. 9; square symbols, ref. 13) in the central Nepal Himalaya. **b** Steepness index k_{sn} along the Marsyandi Valley in central Nepal with an assumed concavity of 0.45 (ref. 10). **c** Thermochronologic ages of ^{40}Ar/^{39}Ar data in the central Nepal Himalaya (triangle symbols; refs. 8,9), and Apatite fission track (AFT) along the Sutlej Valley, NW India (cycle symbols; ref. 11) and along the Marsyandi River catchment, Nepal (square symbols; ref. 15). **d** The observed two-step morphology with two rainfall peaks in the central Nepal Himalaya. Topography is derived from the Shuttle Radar Topography Mission (SRTM) 3 arc second (~90 m) digital elevation model (DEM). Precipitation is calculated from the Tropical Rainfall Measurement Mission (TRMM) data[33]. **e** The geological structures beneath the Himalayas, modified from *Earth Planet Sc Lett*, Vol. 367, Caldwell, W. B., Klemperer, S. L., Lawrence, J. F., Rai, S. S. & Ashish[50], Characterizing the Main Himalayan Thrust in the Garhwal Himalaya, India with receiver function CCP stacking, Pages 15-27, Copyright (2013), with permission from Elsevier, and *Nat Geosci*, Vol. 9, Gao, R. et al.[51]. Crustal-scale duplexing beneath the Yarlung Zangbo suture in the western Himalaya, Pages 555-561, Copyright (2016), with permission from Springer Nature. KF, Karakoram Fault; JT, Jungbwa Thrust; GMD, Gurla Mandhata Detachment; STD, South Tibet Detachment; MBT, Main Boundary Thrust; MCT, Main Central Thrust, and MCT_G and MCT_K are MCT in Garhwal and Karnali/Burang sectors of the Himalayas, respectively. **f, g** Modeled results at 36 Myr (the youthful stage), adopted from Fig. 3b. Fault names are changed accordingly for comparison with the Himalayas: new fault−MBT; old fault 1−PT_2 (Physiographic Transition 2, ref. 10) or MT (Munsiari Thrust, ref. 11); old fault 2−MCT. Olive lines represent approximately the location of these faults. Our models reproduce spatial first-order patterns of deformation, precipitation, and erosion rates in the Himalayas, while the detailed structures are beyond our scope.

Andes[3]. The modeled orographic impact on rainfall distribution with the dominant wind in the opposite direction of subducting plate motion (Fig. 1b, d) is consistent with the observations in the Central Andes. We show that the outward propagation of the orogenic plateau results in increasingly extreme orographic effects on the leeward side (Fig. 1b, d, Supplementary Figs. S8 and S9), amplifying aridity and reducing exhumation, consistent with observations[4]. Along the eastern flank of the Central Andes, that is exposed to westward directed trade winds, the peak rainfall mainly occurs at the first topographic rise[4,35]. At higher elevations to the west, orographic effects cause a progressive decrease in precipitation.

The SANZ have a high Bm = 0.15–0.48 (ref. 17), that corresponds to an erodibility of $4 \times 10^{-5} - 1.3 \times 10^{-4}$ $m^{0.2}$/yr in our models (Fig. 2d; Supplementary Table S2). Using a high erodibility (5×10^{-5} $m^{0.2}$/yr and Bm = 0.4, Fig. 1f) as an example (with the dominant wind in the opposite direction of subducting plate motion), a small orogen (~100 km) forms in our models, similar to the SANZ, where crustal shortening is largely accommodated by thrusting on the Alpine fault and several reverse back thrusts in its hanging wall[36]. The correlation between precipitation and erosion rates is very strong in this case ($R_{P\dot{e}} \sim 0.9$, Fig. 2d), and rock uplift and erosion rates are also highly correlated ($R_{U\dot{e}} \sim 1$, Fig. 2d), reaching a quasi-steady balance between rock uplift and erosion rates. Previous work suggested that the development of an orographic rain shadow may explain the asymmetric exhumation of the SANZ based on numerical models coupling crustal deformation and an imposed kinematic denudation on one side of orogenic topography[1,5,18]. However, our modeling results show that orographic precipitation with the dominant wind in the direction or the opposite direction of subducting plate motion will form similar structures of orogens resembling the SANZ (Fig. 1e, f). This is likely due to the fact that the specifics of the orographic model produce generally symmetric rainfall patterns and that the tectonic deformation pattern likely dominates the structures of small orogens. Our modeling indicates that given our model setup and specifics of the orographic model, a smaller, equilibrated orogen will tend to be less sensitive to moisture source direction (Fig. 2e, f), whereas a larger, transient-growth orogen of medium erodibility will tend to be more sensitive to this parameter (Fig. 2c, d).

Climatic and tectonic controls on localization of strain and erosion in the Himalayas

The Himalayas feature conflicting data and interpretations regarding the relations among deformation, precipitation, and erosion rates[2,8–15]. We show how the models and correlation evolve in detail for the orogenic plateau of Bm = 2, and then how they compare to observations. The erosion rate correlates well with the rock uplift and precipitation rates (higher $R_{U\dot{e}}$ and $R_{P\dot{e}}$ values) when the fault at the plateau margin is in the old stage (Figs. 2b and 3a). The correlation coefficients ($R_{U\dot{e}}$ and $R_{P\dot{e}}$) reduce suddenly when a new fault initiates (Figs. 2b and 3b). This is because, during phases when topography grows, the landscape is not adjusted to the new uplift pattern with erosion rates lower than uplift rates. Then the correlation increases when the new fault becomes mature (Figs. 2b and 3c) and to the best when the mature fault becomes old again.

For comparison with the Himalayas (Fig. 4f, g), we change accordingly the fault names in our model, but it should be noted that no attempt will be made to model this orogenic system in detail since the geological structures are complex with spatially varying fault spacings (Fig. 4a–e). The more robust characteristics of the models are the spatial patterns of deformation, precipitation, and erosion rates. In our model, the MBT is in the youthful (active) stage, and the Physiographic Transition 2 (PT_2)[10] or the Munsiari Thrust[11] is in the mature (less active) stage (Fig. 4f). Our modeling results show the erosion rate above the PT_2 correlating well with the precipitation rate ($R_{P\dot{e}} \sim 0.8$, Fig. 2b), consistent with the observed pattern of erosion rate (characterized by the steepness index k_{sn}, Fig. 4b) and precipitation rate in central Nepal[10]. The modeling results also demonstrate that the erosion rate correlates with the rock uplift rate above the PT_2 (Fig. 4f), which agrees with the observed pattern of rock uplift and erosion rates in the central Nepal Himalaya (Fig. 4a, ref. 13). Our results also show changes in erosion rates separated by the PT_2 (Fig. 4f), reproducing observations of low and high erosion rates separated by the PT_2 (Fig. 4a, ref. 9).

For the long-term exhumation pattern, our modeling shows that changes in exhumation magnitude are separated by several major faults (Fig. 4f); high exhumation between the PT_2 and the Main Central Thrust (MCT), and much higher exhumation above the MCT. The maximum precipitation is located in the area of high exhumation between the PT_2 and the MCT, in the lower part of the maximum exhumation area. Our modeling results can explain several different exhumation patterns and magnitudes existing in the Himalayas. First, our modeling shows a break in long-term exhumation, with high and low exhumation separated by the PT_2 (Fig. 4f), consistent with a strong break in the observed thermochronologic ages (Fig. 4c) associated with the PT_2 (or a thrust fault) and the orographic enhancement of precipitation (refs. 8,9,11). Second, our modeling demonstrates a spatial difference between the areas of maximum precipitation and maximum exhumation, separated by the MCT (Fig. 4f), which can explain the observed spatial difference between the maximum exhumation above the MCT but the strongest modern precipitation below the MCT (Fig. 4c) (ref. 15). This spatial difference indicates that active faulting may have jumped outward so that high precipitation has advanced with the outward growing topography (ref. 37), while the maximum exhumation occurred backward.

Our modeling suggests good correlations among rock uplift, precipitation, and erosion rates for the propagating fault in the mature stage, but the general correlation coefficient between rock uplift and erosion rates is still lower than 1 (actually, $R_{U\dot{e}} \sim 0.9$ with the medium

erodibility and Bm = 2, Fig. 2d), implying a continuing outward growth of the orogenic plateau. This is consistent with the propagation of thrust faults (e.g., the active MBT since the latest Miocene-Pliocene, and active thrusts in the Himalayan front since the Pliocene) responsible for the continuing growth of the Himalayas, well documented and dated by field investigations[38–40] and with numerical experiments[17]. The continuing outward growth of the Himalayas is also evidenced by the observed two-step morphology[33], a transient state during the development of new faults.

Our modeling results provide a plausible explanation for several conflicting data and interpretations in the Himalayas, which we propose are due to the youthful, mature, or old stage of faults and different locations relative to the old faults. Some locations are in the steady-state phase, while others are in the thrust-propagation phase of the intermediate erodibility orogenic cycle. We show both tectonics and climate synchronizing with erosion rates in the active orogenic plateau, while the main driving force comes from the plate tectonic convergence causing faults to propagate outward. The spatial climatic changes co-evolve with the outward propagation of faults and the growth of topography. Our modeling is consistent with changes in exhumation in southern Tibet due to changes in the loci and rate of rock uplift, suggesting a tectonically imposed southward shift of the topographic divides and orographic precipitation within the Lhasa terrane to their current positions within the Himalayas (ref. 37). Models indicate that previous generations of faults that now locate further northward, which agrees with observations[37]. Our findings are also consistent with the along-strike climatic variations responding to tectonically controlled topographic changes, suggested by the contrasting tectonically driven exhumation patterns in the western and central Nepal Himalayas (ref. 41).

In conclusion, this study presents a model of coupled tectonics, surface process, and orographic precipitation, which shows how deformation, precipitation, and erosion coordinate during orogenic growth. Our modeling provides a plausible explanation for the contrasting views on the tectonic or climatic control of erosion in large active orogens (e.g., the Himalayas), which can be explained by different stages corresponding to the evolution of new outward propagating faults at the margin of the orogen. We demonstrate that the response of orogenic systems to spatiotemporally tectonic and climatic change involves a transient and steady-state component controlled by synchronized feedbacks among rock uplift, orographic precipitation, and erosion rates. Such transient and steady states determine the correlation between tectonics, climate, and erosion, as well as the size and structure of an orogen. By incorporating a dynamic component through the use of our coupled model, our findings complement studies that combine thermochronometric/cosmogenic erosion rate measurements and landscape morphologies[8–15]. Studies using similar approaches with more detailed geological parameters could shed more insights into the growth of mountain belts co-evolving with spatiotemporally tectonic and climate change, and help more quantitatively establish links between tectonics, climate, erosion, topography, and biodiversity.

Methods

We use the two-dimensional arbitrary Langrangian-Eulerian (ALE), finite-element geodynamic model ASPECT (Advanced Solver for Planetary Evolution, Convection, and Tectonics; refs. 21–24), computing thermo-mechanically coupled, incompressible, plane-strain, viscous-plastic creeping flows to investigate orogenic growth during continent-continent collision (Supplementary Fig. S1). The ASPECT is coupled to the two-dimensional landscape evolution model FastScape[25,26], which is further coupled to the orographic precipitation model[28]. FastScape with the orographic precipitation acting on surface processes directly interacts with the thermo-mechanical model, in that any fluvial erosion and deposition feeds back to the thermo-mechanical computation through its effect on gravitational stress redistribution and rheology. The two-way coupling between ASPECT and FastScape works through a back-and-forth transfer of surface velocities and surface topography (ref. 27).

Geodynamic model

The geodynamic code ASPECT assumes an extended Boussinesq approximation with an infinite Prandtl number (i.e., no inertial term) and solves the following conservation equations (refs. 21–24),

$$-\nabla\cdot(2\eta\dot{\varepsilon})+\nabla P=\rho g \tag{1}$$

$$\nabla\cdot u=0 \tag{2}$$

$$\bar{\rho}C_p\left(\frac{\partial T}{\partial t}+u\cdot\nabla T\right)-\nabla\cdot k\nabla T=\bar{\rho}H+\alpha T(u\cdot\nabla P) \tag{3}$$

$$\frac{\partial c_i}{\partial t}+u\cdot\nabla c_i=q_i \tag{4}$$

where Eq. 1 is the conservation of momentum, with the effective viscosity η, the deviator of the strain rate tensor $\dot{\varepsilon}$, the velocity u, the pressure P, the density ρ, and the gravity g. Eq. 2 describes the conservation of mass. Eq. 3 is the conservation of energy where $\bar{\rho}$ is the reference adiabatic density, C_p the specific heat capacity, T the temperature, k the thermal conductivity, H the radiogenic heating, and α the thermal expansivity. As right-hand-side heating terms, we include radioactive heating and adiabatic heating, respectively. Eq. 4 is the advection equation for each compositional field c_i (e.g., upper crust, sediment age, and accumulated plastic strain), with reaction rate q_i nonzero for the plastic strain, viscous strain, and sediment age fields.

The model uses a viscoplastic rheology that includes both plastic and viscous weakening[24]. The viscous portion of the model is a harmonically averaged composite of diffusion and dislocation creep (Supplementary Table S1) following refs. 24,42:

$$\eta_{diff|dis}=0.5A_{diff|dis}^{-1/n}d^{m}\dot{\varepsilon}_e^{(1-n)/n}\exp\left(\frac{E_{diff|dis}+PV_{diff|dis}}{nRT}\right) \tag{6}$$

where $A_{diff|dis}$ is the pre-exponential factor rescaled from uniaxial experiments (diff: diffusion, dis: dislocation). n, d, and m are the stress exponent, the grain size, and grain-size exponent, respectively, with $n=1$ for the diffusion creep case and $m=0$ for the dislocation creep case. $\dot{\varepsilon}_e$ is the effective deviatoric strain rate. $E_{diff|dis}$ and $V_{diff|dis}$ are the energy and volume of activation, respectively. P, R, and T are the pressure, the gas constant, and the temperature, respectively.

When the stress is higher than the yield stress, plastic deformation occurs which is described by the Drucker-Prager yield criterion:

$$\sigma_y=C\cos(\phi)+P\sin(\phi) \tag{7}$$

where C is the cohesion, P is the pressure, and ϕ is the internal friction angle. The effective plastic viscosity is then calculated by:

$$\eta_{plas}=\frac{\sigma_y}{2\dot{\varepsilon}_e} \tag{8}$$

To simulate plastic weakening, the friction angle is weakened by 75% from an initial value of 20° to 5.2° as plastic strain accumulates over the interval of 0 to 1. Viscous weakening reduces the pre-exponential factor by 75% over an accumulated viscous strain interval of 0 to 1.

Landscape evolution model

FastScape solves for stream power river incision, sediment transport and deposition in rivers, hillslope diffusion, and filling of local depressions, that is, lakes and mountain foreland basins. It changes the topographic elevation through uplift, the stream-power law (SPL) fluvial erosion, sediment transport and deposition, and hillslope diffusion (refs. 25,26), which are described by

$$\frac{dh}{dt} = U - KA^m S^n + \frac{G}{A}\int_A \left(U - \frac{dh}{dt}\right) dA + K_d \nabla^2 h \tag{9}$$

where h is the topographic elevation (m), U is the uplift rate (m/yr), K is the erosion efficiency ($m^{1\text{-}2m}$/yr), A is the drainage area (m^2), S is the local slope in the steepest-descent direction of water flow (dimensionless), m is the drainage area exponent, n is the slope exponent, G is the deposition coefficient (dimensionless), and K_d is the diffusion coefficient (m^2/yr). In the following, we use $m = 0.4$, $n = 1$ (ref. 30), and $G = 1$ following previous studies[26,43]. The fluvial erosion efficiency K_f is expressed by[29]:

$$K = K_f \tilde{p}^m \tag{10}$$

where K_f is bedrock erodibility that is independent of rainfall, but still encapsulates several factors including rock properties. $\tilde{p} = \bar{P}/P_0$ is the ratio of the upstream average mean precipitation $\bar{P}$ relative to a referential precipitation $P_0 = 1$ m/yr (ref. 44). Therefore, the overall erosion efficiency (i.e., K) consists of two main parts, including non-precipitation erodibility (i.e., lithologies and other minor erosion factors) and precipitation rate. The erodibility K_f is characterized by large uncertainty and spans a wide range, as it incorporates variations as a function of rock type, vegetation, and abrasive agents. Typical values lie between 10^{-7} and 10^{-4} $m^{0.2}$/yr (refs. 30–32), assuming $m = 0.4$ and $n = 1$. We designed three models with low $K_f = 1 \times 10^{-6}$ $m^{0.2}$/yr, medium $K_f = 1 \times 10^{-5}$ $m^{0.2}$/yr, and high $K_f = 5 \times 10^{-5}$ $m^{0.2}$/yr. The hillslope diffusion coefficient is constant with $K_d = 1 \times 10^{-2}$ m^2/yr.

Orographic precipitation model

We use the orographic precipitation model (i.e., the linear feedback precipitation model; ref. 28), which considers spatially variable water contents and the respective fluxes (cloud water and hydrometeors) transported at a given wind velocity, and flux condensation and fallout over long distances. The governing equations of the model are as follows:

$$\frac{-\partial F_v}{\partial x} + L_d \frac{\partial^2 F_v}{\partial y^2} - \frac{F_v - \beta F_c}{L_c} + \epsilon \frac{F_c}{L_f} = 0 \tag{11a}$$

$$\frac{-\partial F_c}{\partial x} + L_d \frac{\partial^2 F_c}{\partial y^2} + \frac{F_v - \beta F_c}{L_c} - \frac{F_c}{L_f} = 0 \tag{11b}$$

$$\beta = \left(1 - \frac{L_c}{L_l}\right)\left(\frac{L_l}{L_f} - 1\right) e^{-\frac{H}{H_0}} \tag{12}$$

$$P = (1 - \epsilon)\frac{F_c}{L_f} + P_b \tag{13}$$

where the subscript v/c means the relation for vapor (v) or cloud water (c), F is the advective flux (m^2/yr), L_d is the dispersion length of precipitation (m), L_c is the condensation length of vapor to cloud water (m), β is an equilibrium coefficient (dimensionless), L_f is the fallout length of cloud water (m), L_l is the decay length of precipitation (m), H_0 is the reference height used in the precipitation model, ϵ is the evapotranspiration fraction (dimensionless), P is the precipitation rate (m/yr), and P_b is the background precipitation rate (m/yr), representing the precipitation rate contributed by other sources (e.g., local lakes) in the orographic precipitation model. Eq. 11 describes vertically integrated moisture balance for each component, Eq. 12 reflects condensation of vapor and re-evaporation of cloud water as competing processes, and Eq. 13 describes the expression of precipitation rate.

By changing the precipitation rate P (Eq. 13) to the upstream average mean precipitation $\bar{P}$ and the variability $\tilde{p} = \bar{P}/P_0$, we couple the above orographic precipitation model to the landscape evolution model (Eq. 10). In this work, we use the total influx 0.8 km^2/yr of vapor and cloud water from the dominant wind boundary in the direction or in the opposite direction of subducting plate motion, the length scale L_c and L_f are both 25 km, the length scale of the decay L_l is 375 km, the dispersion length L_d is 25 km, the evapotranspiration fraction ϵ is 50%, and the background precipitation rate P_b is 0.1 m/yr. We chose this parameter setting[45] as it produces a good match with the observed precipitation rates in the Himalayas (ref. 33).

Pearson correlation analysis

Pearson correlation analysis calculates a correlation coefficient that measures linear correlation between two sets of data. When applied to a sample, it is commonly represented by R_{xy} and may be referred to as the sample correlation coefficient or the sample Pearson correlation coefficient. Given paired data $\{(x_1, y_1), (x_2, y_2), \ldots, (x_n, y_n)\}$ consisting of n pairs, R_{xy} is defined as

$$R_{xy} = \frac{\sum_{i=1}^{n}(x_i - \bar{x})(y_i - \bar{y})}{\sqrt{\sum_{i=1}^{n}(x_i - \bar{x})^2}\sqrt{\sum_{i=1}^{n}(y_i - \bar{y})^2}} \tag{14}$$

where x_i, y_i are the individual sample points indexed with i, $\bar{x} = \frac{1}{n}\sum_{i=1}^{n} x_i$ and $\bar{y} = \frac{1}{n}\sum_{i=1}^{n} y_i$ are the sample mean for x_i and y_i sample points, respectively.

It is the ratio between the covariance of two variables and the product of their standard deviations; thus, it is essentially a normalized measurement of the covariance, such that the result always has a value between −1 and 1. The correlation sign is determined by the R_{xy} value: a value of 1 implies that all data points lie on a line for which y increases as x increases, and vice versa for −1. A value of 0 implies that there is no linear dependency between the variables. In this work, we calculate the Pearson correlation coefficient $R_{U\dot{e}}$ for the uplift rate U and the erosion rate $\dot{e}$, and the correlation coefficient $R_{P\dot{e}}$ for the precipitation rate P and the erosion rate $\dot{e}$.

Model limitations

Some limitations have to be kept in mind when interpreting our model results. First, we assume a constant boundary influx of vapor and cloud water in the precipitation model and a constant convergence rate in the tectonic model, whereas it is well known that the long-term Asian climate changes over time[46] and that the convergence rate varies between the Indian and Eurasian plates[47]. Our models also do not compare quantitatively the magnitudes of precipitation observed in the Central Andes and the SANZ, which would require changing the influx and length-scale parameters of the reference orographic model. Second, to simplify our modeling, the threshold effect of fluvial erosion, in which extreme events may dominate the precipitation and water discharge[48], is not considered in our long-term fluvial erosion-deposition model and precipitation model. Last but not least, our model does not consider the influence of glaciers in high-elevation domains where glaciers are likely more efficient erosion agents than rivers[2,49]. Nevertheless, this study shows agreement with the first-order observed pattern of orogenic growth with dynamic interaction among deformation, orographic precipitation, and erosion.

Data availability

All data supporting the conclusions and findings of this study are contained within the article and the Supplementary Information.

Code availability

Numerical models are computed with published methods and codes, described in the Methods and Supplementary Information. The geodynamic model ASPECT can be obtained from https://github.com/geodynamics/aspect. The landscape evolution model FastScape can be downloaded from https://github.com/fastscape-lem/fastscape and is fully documented at https://fastscape.readthedocs.io/en/latest/. The orographic precipitation model LFPM can be accessed from http://jura.geologie.uni-freiburg.de/openlem/lfpm.php.

References

1. Willett, S. D. Orogeny and orography: the effects of erosion on the structure of mountain belts. *J. Geophys Res-Sol. Ea* **104**, 28957–28981 (1999).
2. Whipple, K. X. The influence of climate on the tectonic evolution of mountain belts. *Nat. Geosci.* **2**, 97–104 (2009).
3. DeCelles, P. G. & Carrapa, B. Differences between the central Andean and Himalayan orogenic wedges: a matter of climate. *Earth. Planet. Sci. Lett* **616**, 118216 (2023).
4. Evenstar, L. A., Hartley, A. J. & Mather, A. E. Orogenic-orographic feedback and the rise of the Central Andes. *Earth Planet Sci. Lett.* **602**, 117931 (2023).
5. Lang, K. A., Glotzbach, C., Ring, U., Kamp, P. J. J. & Ehlers, T. A. Linking orogeny and orography in the Southern Alps of New Zealand: new observations from detrital fission-track thermochronology of the Waiho-1 borehole. *Earth Planet Sci. Lett.* **552**, 116586 (2020).
6. Masek, J. G., Isacks, B. L., Gubbels, T. L. & Fielding, E. J. Erosion and tectonics at the margins of continental plateaus. *J. Geophys Res-Sol. Ea* **99**, 13941–13956 (1994).
7. Beaumont, C., Jamieson, R. A., Nguyen, M. H. & Lee, B. Himalayan tectonics explained by extrusion of a low-viscosity crustal channel coupled to focused surface denudation. *Nature* **414**, 738–742 (2001).
8. Wobus, C. W., Hodges, K. V. & Whipple, K. X. Has focused denudation sustained active thrusting at the Himalayan topographic front? *Geology* **31**, 861–864 (2003).
9. Wobus, C., Heimsath, A., Whipple, K. & Hodges, K. Active out-of-sequence thrust faulting in the central Nepalese Himalaya. *Nature* **434**, 1008–1011 (2005).
10. Hodges, K. V., Wobus, C., Ruhl, K., Schildgen, T. & Whipple, K. Quaternary deformation, river steepening, and heavy precipitation at the front of the Higher Himalayan ranges. *Earth Planet Sc. Lett.* **220**, 379–389 (2004).
11. Thiede, R. C., Bookhagen, B., Arrowsmith, J. R., Sobel, E. R. & Strecker, M. R. Climatic control on rapid exhumation along the Southern Himalayan Front. *Earth Planet Sc. Lett.* **222**, 791–806 (2004).
12. Grujic, D. et al. Climatic forcing of erosion, landscape, and tectonics in the Bhutan Himalayas. *Geology* **34**, 801–804 (2006).
13. Godard, V. et al. Dominance of tectonics over climate in Himalayan denudation. *Geology* **42**, 243–246 (2014).
14. Adams, B. A., Whipple, K. X., Forte, A. M., Heimsath, A. M. & Hodges, K. V. Climate controls on erosion in tectonically active landscapes. *Sci. Adv.* **6**, eaaz3166 (2020).
15. Burbank, D. W. et al. Decoupling of erosion and precipitation in the Himalayas. *Nature* **426**, 652–655 (2003).
16. Wolf, S. G., Huismans, R. S., Munoz, J. A., Curry, M. E. & van der Beek, P. Growth of collisional orogens from small and cold to large and hot - Inferences from geodynamic models. *J. Geophys. Res-Sol Earth.* **126**, e2020JB021168 (2021).
17. Wolf, S. G., Huismans, R. S., Braun, J. & Yuan, X. P. Topography of mountain belts controlled by rheology and surface processes. *Nature* **606**, 516–521 (2022).
18. Koons, P. O., Norris, R. J., Craw, D. & Cooper, A. F. Influence of exhumation on the structural evolution of transpressional plate boundaries: an example from the Southern Alps, New Zealand. *Geology* **31**, 3–6 (2003).
19. Bahadori, A. et al. Coupled influence of tectonics, climate, and surface processes on landscape evolution in southwestern North America. *Nat. Commun* **13**, 4437 (2022).
20. Beaumont, C., Fullsack, P. & Hamilton, J. Erosional control of active compressional orogens. In *Thrust tectonics*, (ed. McClay, K. R.) 1–18 https://doi.org/10.1007/978-94-011-3066-0_1 (Springer, 1992).
21. Kronbichler, M., Heister, T. & Bangerth, W. High accuracy mantle convection simulation through modern numerical methods. *Geophys J. Int* **191**, 12–29 (2012).
22. Heister, T., Dannberg, J., Oller, R. G. & Bangerth, W. High accuracy mantle convection simulation through modern numerical methods - II: realistic models and problems. *Geophys J. Int* **210**, 833–851 (2017).
23. Gassmöller, R., Lokavarapu, H., Heien, E., Puckett, E. G. & Bangerth, W. Flexible and scalable particle-in-cell methods with adaptive mesh refinement for geodynamic computations. *Geochem Geophy Geosy* **19**, 3596–3604 (2018).
24. Glerum, A., Thieulot, C., Fraters, M., Blom, C. & Spakman, W. Nonlinear viscoplasticity in ASPECT: benchmarking and applications to subduction. *Solid Earth* **9**, 267–294 (2018).
25. Braun, J. & Willett, S. D. A very efficient O(n), implicit and parallel method to solve the stream power equation governing fluvial incision and landscape evolution. *Geomorphology* **180**, 170–179 (2013).
26. Yuan, X. P., Braun, J., Guerit, L., Rouby, D. & Cordonnier, G. A new efficient method to solve the stream power law model taking into account sediment deposition. *J. Geophys Res-Earth Surf.* **124**, 1346–1365 (2019).
27. Neuharth, D. et al. Evolution of rift systems and their fault networks in response to surface processes. *Tectonics* **41**, e2021TC007166 (2022).
28. Hergarten, S. & Robl, J. The linear feedback precipitation model (LFPM 1.0) - a simple and efficient model for orographic precipitation in the context of landform evolution modeling. *Geosci. Model Dev.* **15**, 2063–2084 (2022).
29. Ferrier, K. L., Huppert, K. L. & Perron, J. T. Climatic control of bedrock river incision. *Nature* **496**, 206–209 (2013).
30. Stock, J. D. & Montgomery, D. R. Geologic constraints on bedrock river incision using the stream power law. *J. Geophys Res-Sol. Ea* **104**, 4983–4993 (1999).
31. Hilley, G. E. et al. Earth's topographic relief potentially limited by an upper bound on channel steepness. *Nat. Geosci.* **12**, 828–833 (2019).
32. Kirby, E. & Whipple, K. Quantifying differential rock-uplift rates via stream profile analysis. *Geology* **29**, 415–418 (2001).
33. Bookhagen, B. & Burbank, D. W. Toward a complete Himalayan hydrological budget: spatiotemporal distribution of snowmelt and rainfall and their impact on river discharge. *J Geophys Res-Earth Surface* **115**, https://doi.org/10.1029/2009JF001426 (2010).
34. Goren, L., Fox, M. & Willett, S. D. Tectonics from fluvial topography using formal linear inversion: Theory and applications to the Inyo Mountains, California. *J. Geophys Res-Earth Surf.* **119**, 1651–1681 (2014).
35. Bookhagen, B. & Strecker, M. R. Orographic barriers, high-resolution TRMM rainfall, and relief variations along the eastern Andes. *Geophys Res Lett* **35** (2008).
36. Herman, F., Cox, S. C. & Kamp, P. J. J. Low-temperature thermochronology and thermokinematic modeling of deformation, exhumation, and development of topography in the central Southern

Alps, New Zealand. *Tectonics* **28**, https://doi.org/10.1029/2008TC002367 (2009).
37. Tremblay, M. M. et al. Erosion in southern Tibet shut down at ~10 Ma due to enhanced rock uplift within the Himalaya. *P Natl Acad. Sci. USA* **112**, 12030–12035 (2015).
38. DeCelles, P. G. et al. Stratigraphy, structure, and tectonic evolution of the Himalayan fold-thrust belt in western Nepal. *Tectonics* **20**, 487–509 (2001).
39. Huyghe, P., Galy, A., Mugnier, J. L. & France-Lanord, C. Propagation of the thrust system and erosion in the Lesser Himalaya: Geochemical and sedimentological evidence. *Geology* **29**, 1007–1010 (2001).
40. Li, Y. L. et al. Propagation of the deformation and growth of the Tibetan-Himalayan orogen: a review. *Earth-Sci. Rev.* **143**, 36–61 (2015).
41. van der Beek, P. et al. Contrasting tectonically driven exhumation and incision patterns, western versus central Nepal Himalaya. *Geology* **44**, 327–330 (2016).
42. Karato, S. & Wu, P. Rheology of the upper mantle - a synthesis. *Science* **260**, 771–778 (1993).
43. Guerit, L. et al. Fluvial landscape evolution controlled by the sediment deposition coefficient: estimation from experimental and natural landscapes. *Geology* **47**, 853–856 (2019).
44. Yuan, X. P., Guerit, L., Braun, J., Rouby, D. & Shobe, C. M. Thickness of fluvial deposits records climate oscillations. *J. Geophys. Res-Sol Earth* **127**, e2021JB023510 (2022).
45. Li, Y. Q. & Yuan, X. P. Coupled surface process and orographic precipitation model for the landscape evolution of the Himalayas. *J. Earth Sci.* **35**, 1063–1068(2024).
46. Molnar, P., Boos, W. R. & Battisti, D. S. Orographic Controls on Climate and Paleoclimate of Asia: Thermal and Mechanical Roles for the Tibetan Plateau. *Annu. Rev. Earth Planet. Sci.* **38**, 77–102 (2010).
47. Molnar, P. & Stock, J. M. Slowing of India's convergence with Eurasia since 20 Ma and its implications for Tibetan mantle dynamics. *Tectonics* **28**, https://doi.org/10.1029/2008TC002271 (2009).
48. Lague, D., Hovius, N. & Davy, P. Discharge, discharge variability, and the bedrock channel profile. *J. Geophys. Res-Earth* **110**, https://doi.org/10.1029/2008TC002271 (2005).
49. Egholm, D. L., Nielsen, S. B., Pedersen, V. K. & Lesemann, J. E. Glacial effects limiting mountain height. *Nature* **460**, 884–888 (2009).
50. Caldwell, W. B., Klemperer, S. L., Lawrence, J. F., Rai, S. S. & Ashish. Characterizing the main Himalayan thrust in the Garhwal Himalaya, India with receiver function CCP stacking. *Earth Planet Sci. Lett* **367**, 15–27 (2013).
51. Gao, R. et al. Crustal-scale duplexing beneath the Yarlung Zangbo suture in the western Himalaya. *Nat. Geosci.* **9**, 555–561 (2016).

Acknowledgements

The authors are grateful for the discussions with Wenrong Cao, Jianfeng Yang, Anne Glerum, Stefan Hergarten, and Jiashun Hu. X.Y. acknowledges funding from NSFC (Grants 42272261, U23A2023). M.P. is funded by ERC MEET (Grant 856555). S.B. has been funded by the European Union (ERC, EMERGE, 101087245). The authors gratefully acknowledge the computing time granted by the Resource Allocation Board and provided on the supercomputer Lise at NHR@ZIB as part of the NHR infrastructure. The calculations for this research were conducted with computing resources under the project bbp00039.

Author contributions

X.Y., Y.L., S.B., K.L., M.P., and S.G.W. designed the experiments, discussed the results and implications, and wrote the article. With help from Y.L., S.B., K.L., M.P., and S.G.W., X.Y. developed the model of coupled tectonics, surface process, and orographic precipitation. S.B. acquired the computational resources in this study. X.Y. conducted the comparison to natural examples, and ran and visualized the models.

Competing interests

The authors declare no competing interests.

Additional information

Supplementary information The online version contains supplementary material available at https://doi.org/10.1038/s41467-024-54690-4.

Correspondence and requests for materials should be addressed to Xiaoping Yuan.

Peer review information *Nature Communications* thanks Sean Gallen, Jonathan H Tomkin and the other, anonymous, reviewer(s) for their contribution to the peer review of this work. A peer review file is available.